Calibrating and Mosaicking Surface Velocity Measurements from Interferometric SAR Data with a Simultaneous Least-squares Adjustment Approach

Hongxing Liu and Jaehyung Yu

Department of Geography, Texas A&M University, College Station, TX 77843, USA

Email: liu@geog.tamu.edu

jay@geog.tamu.edu

Zhiyuan Zhao

Vexcel Canada Inc., 20 Colonnade Road, Suite 110,

Nepean, Ontario, K2E 7M6, Canada

Email: zhiyuan.zhao@vexcel.com

Kenneth C. Jezek

Byrd Polar Research Center, The Ohio State University, Columbus, OH 43210, USA

Email: jezek@frosty.mps.ohio-state.edu

International Journal of Remote Sensing

Calibrating and Mosaicking Surface Velocity Measurements from Interferometric SAR Data with a Simultaneous Least-squares Adjustment Approach

Abstract.

The repeat-pass interferometric SAR (InSAR) technique has been well established as a precise means to extract two-dimensional surface velocity fields. Many applications require velocity measurements over a large area and multiple InSAR image frames from the same and/or adjacent orbits are needed to achieve full ground coverage. The conventional frame-by-frame processing approach often causes velocity discrepancies and discontinuities between adjacent frames. In addition, absolute velocity information may not be derived for some image frames due to a lack of velocity control points. We present a unified simultaneous least-squares adjustment method for calibrating and merging surface displacements derived from multiple InSAR image frames. Observation equations have been mathematically derived for velocity control points, flow direction control points, and tie points. The major advantages of our method include consistent and smooth transition of velocity measurements between adjacent frames and dramatic reduction of velocity control point requirements. For those frames devoid of velocity control points, absolute velocity measurements can still be derived with this method based on distant velocity control points in other frames or motion direction constraints imposed by surface flow stripes. The benefits of our method are demonstrated and evaluated by using Radarsat InSAR data for Antarctica acquired in 1997.

Calibrating and Mosaicking Surface Velocity Measurements from Interferometric SAR Data with a Simultaneous Least-squares Adjustment Approach

1. Introduction

The ice flow direction and magnitude are instrumental in the re-distribution of ice mass within a drainage basin. Knowledge of ice flow velocity is important in assessing ice mass balance and in understanding the flow dynamics of ice streams and glaciers (Gray *et al.* 2001, Zhao 2001, Rignot 2002). With the development of the Global Positioning System (GPS) and spaceborne remote sensing technology, the ice surface motion can be efficiently and precisely measured and monitored. Highly accurate *in-situ* velocity observations can be made by using the differential GPS techniques (Kiernan 1998, King *et al.* 2000, Hamilton and Whillans 2000). However, velocity data from the repeat GPS measurements are often very sparse and cover a limited areal extent, because of logistical difficulties and corresponding high cost of field surveys. Spaceborne remote sensing data are well suited to derive broad, dense spatial coverage of surface velocity information.

Three methods have been developed to extract surface velocity measurements from remotely sensed data. Those include a feature retracking method (Scambos *et al*. 1992), a phase unwrapping method (Goldstein *et al.* 1993) and a speckle tracking method (Gray *et al.* 1998). The feature retracking method is based on a pair of sequential optical (Lucchita and Ferguson 1986, Bindschadler and Scambos 1991, Scambos *et al.* 1992) or radar (Fahnestock *et al.* 1993) images acquired at different times. It measures the displacements of surface features between two image acquisitions through an automated image matching algorithm. Because the presence of identifiable features is a prerequisite for successful image matching, this method often fails to generate velocity measurements for large and featureless ice surfaces. Both the phase

unwrapping method and speckle tracking method are based on repeat-pass interferometric Synthetic Aperture Radar (SAR) images. Since the launch of the ERS-1 satellite in 1991, the repeat-pass interferometric SAR (InSAR) technique has emerged as a precise means to derive detailed and accurate measurements of surface motion (Joughin *et al.* 1996, 1999a, Kowk and Fahnestock 1996, Rignot 1996, Mohr *et al.* 1998, Frolich and Doake 1998, Fatland and Lingle 1998, Stenoien and Bentley 2000). The phase unwrapping method, first demonstrated by Glodstein *et al.* (1988, 1993), has been well established. The speckle tracking method, also known as speckle matching or speckle correlation, has developed as an alternative approach for processing repeat-pass interferometric SAR data for the surface velocity (Gray *et al.* 1998, Michel and Rignot 1999, Joughin *et al.* 1999b, Zhao 2001, Joughin 2002). It is particularly suitable for InSAR data with long repeat cycles and areas with high surface motion speed.

An InSAR image frame acquired by ERS-1, ERS-2 or Radarsat-1 SAR sensor normally covers a ground area of 100 km by 100 km. Many applications require surface velocity data over a wider area. Multiple InSAR image frames from the same or adjacent orbits are required to achieve a full coverage. Conventionally, InSAR image data were processed separately frame by frame. As a consequence of independent processing, velocity measurements obtained from one InSAR image frame are generally different from those obtained from other adjacent InSAR frames for the overlapping region. When the velocity data derived from individual image frames are merged, inconsistency and discontinuity in the surface motion speed and direction between neighboring frames are bound to occur. In addition, no matter whether the phase unwrapping method or speckle tracking method is used, velocity control points are required to calibrate the relative surface displacements from the InSAR data to absolute velocity estimates. Commonly, rock outcrops are conveniently selected as zero velocity control points for this purpose. Such

velocity control points may not be identified for some InSAR image frames, which preclude the derivation of absolute velocity information.

In this paper, we present a simultaneous least-squares adjustment method for calibrating and merging surface motion measurements obtained from multiple InSAR image frames. Based on a limited number of velocity control points and a set of velocity tie points, our method simultaneously calibrates model parameters and determines surface displacement measurements for all frames in a strip or a block. With this method, the velocity discrepancies between adjacent image frames are minimized, and a seamless velocity mosaic can be produced. In addition, this method greatly relaxes the velocity control point requirements. For those frames devoid of velocity control points, absolute velocity measurements can still be derived by utilizing distant velocity control points in other image frames or by utilizing the flow direction constraints imposed by surface flow stripes.

In the following sections, we first review the phase unwrapping method and speckle tracking method for processing interferometric SAR data, with a brief discussion on their comparative advantages. Then, we present the mathematical formulation of observation equations for the simultaneous least-squares adjustment of multiple InSAR frames. Next, we demonstrate the benefits and evaluate the performance of the simultaneous least-squares adjustment method using Radarsat InSAR data for Antarctica acquired in 1997. In the final section, we draw some conclusions.

2. Derivation of surface displacement measurements from individual InSAR frames

The repeat-pass interferometric SAR data consists of two or more complex radar images for the same scene acquired by a SAR sensor in a precise repeat orbit. The scene is imaged from almost

the same geometry, but with slightly different positions and aspect angles during different passes of the spacecraft. The phase unwrapping method and speckle tracking method represents two different schemes to measure surface displacements based on the repeat-pass InSAR data. Along with the known time span of the repeat cycle, the derived surface displacements can be converted to the measurements for surface motion speed and direction.

The phase unwrapping method measures the phase differences between the complex radar images. If the ground is not seriously disturbed between passes, two complex radar images can be correlated to form an interferogram. The phase measured from the interferogram includes contributions from both the topography effect and the surface motion effect. Using a digital elevation model, the topography-induced phase can be removed, resulting in fringe patterns solely due to surface motion. When more than two passes of SAR data are available, differential interferometry can be used to separate the surface motion component from the topography component by a double difference technique (Kwok and Fahnestock 1996, Joughin *et al.* 1996a). After performing the phase unwrapping operation, the absolute phase measurements can be converted to surface displacements in the radar line-of-sight (LOS) direction. The accuracy of the resulting displacement measurement at each pixel is highly accurate, at a fraction of the radar signal wavelength. Under the assumption that the ice flow vector is parallel to the ice surface, the radial LOS velocity can be projected into horizontal surface velocities with an estimate of the flow direction from a digital elevation model (DEM) (Kwok and Fahnestock 1997). With two InSAR pairs respectively from ascending and descending passes, three-dimensional surface displacements can be solved at an improved accuracy without using the surface parallel flow assumption (Kwok and Fahnestock, 1996, Joughin *et al.* 1998, Mohr *et al.* 1998, Joughin 2002, Gray *et al.* 2005).

For one interferometric SAR pair, the surface motion induced phase component (Φ_m) in the LOS direction can be expressed as (Zhao 2001):

$$\Phi_m = \Phi - \Phi_0 \qquad (1)$$

where Φ is the unwrapped phase after the removal of the topography effect, and Φ_0 is an unknown constant phase, which is caused by the arbitrary selection of an initial start point for phase unwrapping. The surface motion velocity (V_r) in the range (cross-track) direction can be calculated by Equation (2):

$$V_r = \frac{\lambda}{4\pi T \sin(\beta + \alpha_r)} \Phi_m = \frac{\lambda}{4\pi T \sin(\beta + \alpha_r)} (\Phi - \Phi_0) \qquad (2)$$

where λ is the wavelength of radar signal, T is the time interval between acquisitions, β is the incidence angle, and α_r is the surface slope angle in the range (cross-track) direction. The geometry parameters of interferometry are illustrated in figure 1.

(Insert figure 1 near here)

The speckle tracking method measures surface displacements by correlating and tracking the image speckle patterns between two repeat-pass acquisitions (Gray et al. 1998). A correlation matching algorithm is commonly used to obtain both azimuth (along-track) and range (across-track) direction offsets based on the coherent speckle pattern of small chips of the InSAR image pair. The cross-correlation can be performed using the real-valued amplitude images or the complex-valued radar images (Gray *et al.* 2001, Young and Hyland 2002, Joughin 2002). For low-correlation regions, the cross-correlation surface from the complex-valued radar images is more strongly peaked, and hence more accurate matches can be achieved with a relatively small chip size. In regions with shear or steep topography, however, large phase gradients across the image chips often fail the match by reducing or eliminating the correlation peak. In such regions,

the cross-correlation based on the amplitude radar images is unaffected by the phase gradients and can generate reliable offset estimates. Through oversampling of the correlation surface, the matching peak can be determined to a small fraction of a pixel spacing, resulting in accurate estimates of the surface displacements. It should be noted that the speckle tracking method does not depend on visible features in the images and is normally much more accurate than the feature retracking method, which depends on visible and identifiable features. The topography induced range offset component can be removed by using a digital elevation model. The range offset (δ_r) after the removal of topography effect and azimuth offset (δ_a) include a non-motion component contributed by the imaging geometry (parallel baseline and orbit squint angle). The non-motion term in the range and azimuth offsets can be modeled using a linear model. The actual surface displacements in the range and azimuth direction can be computed by removing the modeled non-motion term as (Zhao 2001, Joughin 2002):

$$d_r = \delta_r - (a_0 + a_1 x + a_2 y) \qquad (3)$$

$$d_a = \delta_a - (b_0 + b_1 x + b_2 y) \qquad (4)$$

where d_r and d_a are respectively the surface displacements in the range and azimuth directions measured in pixel, x and y are the range and azimuth coordinates of the slant range image, a_0, a_1, and a_2 are coefficients of the linear model, which account for the non-motion term in range direction, and, b_0, b_1, and b_2 are coefficients of the linear model, which account for the non-motion term in azimuth direction. Parameters a_0 and b_0, are related to the parallel baseline, a_1 and b_1, are related to the orbit squint angle, and a_2 and b_2, are related to the change of the orbit squint angle along the flight line. The velocity components in the range (V_r) and azimuth (V_a) directions can be calculated from the equations below:

$$V_r = \frac{d_r - B\cos(\chi - \theta)}{T\sin(\beta + \alpha_r)} \cdot S_r \qquad (5)$$

$$V_a = \frac{d_a}{T\cos(\alpha_a)} \cdot S_a \qquad (6)$$

where B is the length of the base line, χ is the baseline angle, β is the local incidence angle, θ is the radar look angle, α_r and α_a are terrain slopes respectively in the range and azimuth directions, S_r and S_a are pixel sizes respectively in range and azimuth directions, and T is the time interval between two image acquisitions. The definitions of the above geometric parameters are illustrated in figure 1. Since range pixel size is larger than azimuth pixel size for a slant range SAR image and the range motion estimates are affected by the baseline and topography, the range velocity estimates from the speckle tracking method are much less accurate than the azimuth velocity estimates.

The two-dimensional horizontal velocity field ($\vec{V}$) can be expressed as:

$$\vec{V} = V_r\vec{r} + V_a\vec{a} \qquad (7)$$

where V_r and V_a are the magnitudes of the surface motion speed in the range and azimuth directions, and $\vec{r}$ and $\vec{a}$ are unit vectors in the range and azimuth directions. The surface motion speed (s) and direction (ψ) can be calculated by the following equations:

$$s = \sqrt{V_r^{\,2} + V_a^{\,2}} \qquad (8)$$

$$\psi = \arctan\left(\frac{V_a}{V_r}\right) \qquad (9)$$

The phase unwrapping method and speckle tracking method have their advantages and disadvantages (Joughin *et al.* 1999b, Gray *et al.* 2001, Zhao 2001, Joughin 2002). In fact, they are complementary each other. With one interferometric SAR image pair, the speckle tracking

method can derive two-dimensional surface displacements in both range and azimuth directions, in contrast to the range-only displacement measurement of the phase unwrapping method. For the speckle tracking method, the accuracy requirements for orbit and topographic data are not as stringent as for phase unwrapping method. In fast-moving areas, the high fringe rate of the interferogram may make the phase unwrapping impossible, or the interferogram may be unwrapped into several small and disconnected regions due to the patchy coherence. Since the speckle tracking method is less sensitive to decorrelation and does not require phase unwrapping, it is able to provide displacement measurements farther into the shear margins and across areas with a higher strain rate. In comparison, the primary advantages of the speckle tracking method lie in its ability to estimate surface motion speed and direction with one interferometric data pair and its suitability in areas of high ice velocity and long orbit repeat cycles. The major disadvantage of the speckle tracking method is that its range direction displacement measurements have intrinsically lower resolution and inferior accuracy, compared with the differential phase-based measurements of the phase unwrapping method.

To make full use of the comparative advantages of both methods, the range motion component derived by the phase unwrapping method and the azimuth motion component derived by the speckle matching method should be combined whenever possible (Gray *et al.* 2001, Zhao 2001, Joughin 2002). Coupling the speckle tracking method with the phase unwrapping method creates the two-dimensional horizontal surface velocity field with the best possible accuracy. When no differential phase measurements can be made, for instance, in the case of fast-moving areas or the InSAR data pair with a long temporal baseline, the speckle tracking method is the only possible approach to obtain the measurements of both the range and azimuth motion components.

3. Mathematical formulation of observation equations and unified least-squares adjustment

We propose a simultaneous least-squares adjustment method for calibrating and mosaicking the surface displacement measurements derived from multiple InSAR data pairs in a strip or a block. A strip consists of a sequence of overlapping InSAR data pairs that are acquired from the same orbit. A block comprises a number of overlapping strips of InSAR data. The first step in a least-squares strip or block adjustment is to identify the underlying observation equations, along with the minimum number of constraints (control points) necessary to solve for the adjustment problem. In the simultaneous least-squares adjustment, we incorporate the following types of constraints: velocity control points, flow direction control points, and velocity tie points. The goal of the simultaneous least-squares adjustment is to reduce the number of required control points to a minimum and to produce a consistent and seamless velocity mosaic within a strip or a block. We derive and present mathematical observation equations in two different cases, which are referred to as case 1 and case 2 in the following sections. In case 1, the speckle tracking method alone is used to derive both range and azimuth displacements for the two-dimensional velocity field. Case 1 fits situations where the surface motion is fast and/or the interferometric SAR pair has a long temporal baseline. In case 2, the range displacements derived from the phase unwrapping method are combined with the azimuth displacements derived from the speckle tracking method to calculate the two-dimensional velocity field. As discussed above, case 2 is suitable for the slow moving areas.

3.1 Observation equations for velocity control points

In case 1, Equations (3) and (4) are used to calculate range and azimuth displacements. Six unknown parameters need to be determined, including a_0, a_1, a_2. b_0, b_1, and b_2. In case 2, Equation (1) is used to calculate range displacements while Equation (4) is still used to calculate azimuth displacements. There are four unknown parameters in Equations (1) and (4), including Φ_0, b_0, b_1, and b_2 Once the four parameters are determined, the two-dimensional surface displacements can be calculated.

Velocity control points play an important role in calibrating the unknown parameters. A velocity control point is a feature with a known position and velocity. Namely, its range and azimuth coordinates and its surface displacements in both range and azimuth directions (D_r, D_a) during the orbit repeat cycle are known. For case 1, observation equations for a velocity control point can be derived from Equations (3) and (4) as:

$$a_0 + a_1 x + a_2 y = \delta_r - D_r \qquad (10)$$

$$b_0 + b_1 x + b_2 y = \delta_a - D_a \qquad (11)$$

For case 2, the azimuth observation equation for the velocity control point is the same as equation (11), and the range observation equation can be derived from Equation (1) as:

$$\Phi_0 = \Phi - \frac{4\pi D_r}{\lambda} \qquad (12)$$

In practice, features at rock outcrops are often selected as stationary velocity control points, and their surface displacements are set to zero, namely, D_r=0 and D_a=0. Non-stationary velocity control points can be acquired through *in situ* GPS measurements, but they are often unavailable. Each stationary or non-stationary velocity control point gives rise to two observation equations. The accurate determination of the unknown parameters requires a least-squares calibration with redundant observations. In case 1, a minimum of 4 non-collinear

velocity control points are required to calibrate the six unknown parameters a_0, a_1, a_2. b_0, b_1, and b_2 in observation equations (10) and (11). In case 2, at least 3 non-collinear velocity control points are required to calibrate the four unknown parameters Φ_0, b_0, b_1, and b_2 in observation equations (11) and (12). The quality, number, and spatial distribution of the velocity control points influence the estimates of the unknown parameters and hence the accuracy of the surface displacements. If the velocity control points are well distributed in both the range and azimuth directions, the least-squares solution for the parameters would be more stable and reliable. A larger number of velocity control points can reduce the propagation of errors in the velocity control points.

3.2 Observation equations for flow direction control points

In some cases, no sufficient number of stationary or non-stationary velocity control points can be identified for the least-squares calibration of the unknown parameters. But, we may be able to determine the ice flow direction at many locations using ice flow stripes visible on the SAR images. In this paper, we extend the definition of velocity control points by including the flow direction control points. A flow direction control point is a location whose flow direction angle (ψ) is known, but no information is available for the magnitude of flow speed. The flow direction control point defines a ratio of range motion and azimuth motion by the equation below:

$$\frac{V_a}{V_r} = \tan\psi \qquad (13)$$

where V_r and V_a are range and azimuth direction velocity components, and ψ is the flow directional angle.

(Insert figure 2 about here)

A flow direction control point can be acquired by directly measuring the orientation angle (ψ) of a flow stripe on a SAR image. Nevertheless, it is more convenient and efficient in practice to measure the range and azimuth coordinates of the end points (x_1, y_1) and (x_2, y_2) for a short straight segment along a flow stripe in the slant range SAR image (figure 2). By differencing the range and azimuth coordinates of the two end points, we can obtain the range and azimuth offsets (Δr, Δa) along the flow stripe, which virtually define the flow directional angle.

For case 1, the measured range and azimuth offsets along a flow stripe can be expressed as:

$$k\Delta r = \delta_r - a_0 - a_1 x - a_2 y \qquad (14)$$

$$k\Delta a = \delta_a - b_0 - b_1 x - b_2 y \qquad (15)$$

where k is a constant scaling factor, other parameters are the same as those in Equations (10) and (11). By dividing Equation (15) by Equation (14), we can cancel the scaling factor k and obtain the following observation equation for a flow direction control point:

$$a_0 + a_1 x + a_2 y - \frac{\Delta a}{\Delta r}(b_0 + b_1 x + b_2 y) = \delta_a - \frac{\Delta a}{\Delta r}\delta_r \qquad (16)$$

For case 2, Equation (14) is replaced by the following equation:

$$k\Delta r = \frac{\lambda}{4\pi S_r}(\Phi - \Phi_0) \qquad (17)$$

By dividing Equation (15) by Equation (17), we can cancel the scaling factor k and obtain the following observation equation for case 2:

$$\frac{\lambda \Delta a}{4\pi \Delta r}\Phi_0 - b_0 - b_1 x - b_2 y = \frac{\lambda \Delta a}{4\pi \Delta r}\Phi - \delta_a \qquad (18)$$

Compared with stationary and non-stationary velocity control points, flow direction control points impose relatively weaker constraints on the least-squares adjustment. Each flow

direction control point can only provide one observation equation. In case 1, there are six unknown parameters in observation equation (16), including a_0, a_1, a_2. b_0, b_1, and b_2. At least 7 non-parallel flow direction control points are required for the least-squares solution. In case 2, there are four unknowns in observation equation (18), including Φ_0, b_0, b_1, and b_2. A minimum of 5 non-parallel flow direction control points are required for the least-squares solution for the unknown parameters. For the areas where no rock exposures can be found or no *in situ* velocity measurements are available, the flow stripes visible on SAR images can be used as flow direction control points to form observation equations for the least-squares adjustment. However, caution should be exercised when using flow stripes as direction controls. Although in most cases visible flow stripes indicate the present ice flow directions, they might be relic and hence do not represent current ice flow patterns in some rare situations (Casassa and Brecher 1993).

3.3 Observation equations for tie points and simultaneous adjustment of multiple frames

To obtain a full coverage of velocity measurements for a large area, multiple frames of interferometric SAR data sets from the same or adjacent orbits need to be processed. If interferometric data frames are processed independently, at least 4 non-collinear velocity control points or 7 non-parallel flow direction control points are required for each frame in case 1, and at least 3 non-collinear velocity control points or 5 non-parallel flow direction control points are required for each frame in case 2. If both velocity control points and flow direction control points are available, they can be combined to form the minimum number of observation equations required to calibrate the unknown parameters for each frame. However, absolute velocity measurements cannot be derived for those frames where the number of available control points is fewer than the required minimum. The other serious problem is that, even with an adequate

number of control points for each frame, velocity measurements calculated from neighboring frames often are different for overlapping areas. This is because the accuracy and spatial arrangement of control points vary from frame to frame. When the merged velocity measurements are used in glaciological and geophysical applications, artificial velocity discontinuities between adjacent frames often mislead the numerical analysis. To eliminate velocity discontinuities and to relax the need for a certain number of control points for each frame, we propose the use of velocity tie points to stitch individual interferometric SAR frames together within a strip or a block. Instead of an independent least-squares calibration for a single interferometric SAR image frame at a time, we simultaneously compute unknown parameters for all image frames in a strip or a block by linking individual image frames through tie points.

A tie point refers to the same ground feature that can be recognized in two overlapping images. Tie points can be identified visually or through an automated image matching technique. For a tie point, its velocity can be derived from two different images. Logically, the velocity measurement for a tie point derived from one image frame should be exactly the same as that from the other image. This condition is used as a constraint to derive the observation equations for the tie points. We first limit our discussion to a strip consisting of two overlapping frames, but it can be easily extended to a strip or a block having more than two overlapping image frames.

(Insert figure 3 near here)

As shown in figure 3, tie points are located in the overlap area between two adjacent images *i* and *i+1*. In case 1, we can write two equations for calculating the range and azimuth surface displacements of a tie point based on the first image frame (*i*) as follows:

$$d_r = \delta_r^i - (a_0^i + a_1^i x^i + a_2^i y^i) \qquad (19)$$

$$d_a = \delta_a^i - (b_0^i + b_1^i x^i + b_2^i y^i) \qquad (20)$$

where x^i and y^i are range and azimuth coordinates of the image frame *i*, δ_r^i and δ_a^i are the measured range and azimuth offsets of the tie point from the image frame *i*, and a_0^i, a_1^i, a_2^i, b_0^i, b_1^i, and b_2^i are six unknown parameters for the image frame *i*.

Similarly, we can write two equations for the tie point based on the second image frame (*i+1)* as follows:

$$d_r = \delta_r^{i+1} - (a_0^{i+1} + a_1^{i+1} x^{i+1} + a_2^{i+1} y^{i+1}) \qquad (21)$$

$$d_a = \delta_a^{i+1} - (b_0^{i+1} + b_1^{i+1} x^{i+1} + b_2^{i+1} y^{i+1}) \qquad (22)$$

where x^{i+1} and y^{i+1} are range and azimuth coordinates of the image frame *i+1*, δ_r^{i+1} and δ_a^{i+1} are the measured range and azimuth offsets of the tie point from the image frame *i+1*, and a_0^{i+1}, a_1^{i+1}, a_2^{i+1}, b_0^{i+1}, b_1^{i+1}, and b_2^{i+1} are six unknown parameters for the image frame *i+1*.

By subtracting equation (21) from equation (19) and equation (22) from equation (20), we obtain two observation equations for a tie point in case 1:

$$a_0^i + a_1^i x^i + a_2^i y^i - a_0^{i+1} - a_1^{i+1} x^{i+1} - a_2^{i+1} y^{i+1} = \delta_r^i - \delta_r^{i+1} \qquad (23)$$

$$b_0^i + b_1^i x^i + b_2^i y^i - b_0^{i+1} - b_1^{i+1} x^{i+1} - b_2^{i+1} y^{i+1} = \delta_a^i - \delta_a^{i+1} \qquad (24)$$

In case 2, the azimuth observation equation for a tie point is the same as equation (24). Following Equation (1), we can write two equations to calculate the phase respectively from image frame *i* and frame *i+1* as:

$$\Phi_m = \Phi^i - \Phi_0^i \qquad (25)$$

$$\Phi_m = \Phi^{i+1} - \Phi_0^{i+1} \qquad (26)$$

where Φ^i, Φ^{i+1} are the measured phases from image frame *i* and image frame *i+1*, Φ_0^i and Φ_0^{i+1} are the unknown parameters respectively for image frame *i* and image frame *i+1*. Subtracting Equation (26) from Equation (25), we obtain the range observation equation for a tie point in case 2:

$$\Phi_0^i - \Phi_0^{i+1} = \Phi^i - \Phi^{i+1} \tag{27}$$

Observation equations for velocity control points, flow direction control points, and velocity tie points within a strip or a block can be integrated to perform a unified least-squares calibration of unknown parameters for all image frames. Assume that we have *n* velocity control points and *m* flow direction control points for image frame *i*, *p* velocity control points for image frame *i+1*, and *q* velocity tie points between image frame *i* and image frame *i+1*. Observation equations for a mixture of different types of control points and tie points can be written in a matrix format for case 1 as follows:

$$\begin{bmatrix}
1 & x_1^i & y_1^i & 0 & 0 & 0 & 0 & 0 & 0 & 0 & 0 & 0 \\
0 & 0 & 0 & 1 & x_1^i & y_1^i & 0 & 0 & 0 & 0 & 0 & 0 \\
. & . & . & . & . & . & . & . & . & . & . & . \\
1 & x_n^i & y_n^i & 0 & 0 & 0 & 0 & 0 & 0 & 0 & 0 & 0 \\
0 & 0 & 0 & 1 & x_n^i & y_n^i & 0 & 0 & 0 & 0 & 0 & 0 \\
1 & 1 & 1 & -\frac{\Delta a_{n+1}^i}{\Delta r_{n+1}^i} & -\frac{\Delta a_{n+1}^i}{\Delta r_{n+1}^i} x_{n+1}^i & -\frac{\Delta a_{n+1}^i}{\Delta r_{n+1}^i} y_{n+1}^i & 0 & 0 & 0 & 0 & 0 & 0 \\
. & . & . & . & . & . & . & . & . & . & . & . \\
1 & 1 & 1 & -\frac{\Delta a_{n+m}^i}{\Delta r_{n+m}^i} & -\frac{\Delta a_{n+m}^i}{\Delta r_{n+m}^i} x_{n+m}^i & -\frac{\Delta a_{n+m}^i}{\Delta r_{n+m}^i} y_{n+m}^i & 0 & 0 & 0 & 0 & 0 & 0 \\
0 & 0 & 0 & 0 & 0 & 0 & 1 & x_{n+m+1}^{i+1} & y_{n+m+1}^{i+1} & 0 & 0 & 0 \\
0 & 0 & 0 & 0 & 0 & 0 & 0 & 0 & 0 & 1 & x_{n+m+1}^{i+1} & y_{m+n+1}^{i+1} \\
. & . & . & . & . & . & . & . & . & . & . & . \\
0 & 0 & 0 & 0 & 0 & 0 & 1 & x_{n+m+p}^{i+1} & y_{n+m+p}^{i+1} & 0 & 0 & 0 \\
0 & 0 & 0 & 0 & 0 & 0 & 0 & 0 & 0 & 1 & x_{n+m+p}^{i+1} & y_{n+m+p}^{i+1} \\
1 & x_{n+m+p+1}^i & y_{n+m+p+1}^i & 0 & 0 & 0 & -1 & -x_{n+m+p+1}^{i+1} & -y_{n+m+p+1}^{i+1} & 0 & 0 & 0 \\
0 & 0 & 0 & 1 & x_{n+m+p+1}^i & y_{n+m+p+1}^i & 0 & 0 & 0 & -1 & -x_{n+m+p+1}^{i+1} & -y_{n+m+p+1}^{i+1} \\
. & . & . & . & . & . & . & . & . & . & . & . \\
1 & x_{n+m+p+q}^i & y_{n+m+p+q}^i & 0 & 0 & 0 & -1 & -x_{n+m+p+q}^{i+1} & -y_{n+m+p+q}^{i+1} & 0 & 0 & 0 \\
0 & 0 & 0 & 1 & x_{n+m+p+q}^i & y_{n+m+p+q}^i & 0 & 0 & 0 & -1 & -x_{n+m+p+q}^{i+1} & -y_{n+m+p+q}^{i+1}
\end{bmatrix}
\bullet
\begin{bmatrix}
a_0^i \\ a_1^i \\ a_2^i \\ b_0^i \\ b_1^i \\ b_2^i \\ a_0^{i+1} \\ a_1^{i+} \\ a_2^{i+1} \\ b_0^{i+1} \\ b_1^{i+1} \\ b_2^{i+1}
\end{bmatrix}
=
\begin{bmatrix}
\delta_{r_1}^i - D_{r_1}^i \\
\delta_{a_1}^i - D_{a_1}^i \\
\cdots \\
\delta_{r_n}^i - D_{r_n}^i \\
\delta_{a_n}^i - D_{a_n}^i \\
\delta_{a_{n+1}}^i - \frac{\Delta a_{n+1}^i}{\Delta r_{n+1}^i} \delta_{r_{n+1}}^i \\
\cdots \\
\delta_{a_{n+m}}^i - \frac{\Delta a_{n+m}^i}{\Delta r_{n+m}^i} \delta_{r_{n+m}}^i \\
\delta_{r_{n+m+1}}^{i+1} - D_{r_{n+m+1}}^{i+1} \\
\delta_{a_{n+m+1}}^{i+1} - D_{a_{n+m+1}}^{i+1} \\
\cdots \\
\delta_{r_{n+m+p}}^{i+1} - D_{r_{n+m+p}}^{i+1} \\
\delta_{a_{n+m+p}}^{i+1} - D_{a_{n+m+p}}^{i+1} \\
\delta_{r_{n+m+p+1}}^i - \delta_{r_{n+m+p+1}}^{i+1} \\
\delta_{a_{n+m+p+1}}^i - \delta_{a_{n+m+p+1}}^{i+1} \\
\cdots \\
\delta_{r_{n+m+p+1}}^i - \delta_{r_{n+m+p+1}}^{i+1} \\
\delta_{a_{n+m+p+1}}^i - \delta_{a_{n+m+p+1}}^{i+1}
\end{bmatrix} \tag{28}$$

Similarly, we can write the observation equations in matrix format for case 2 as follows:

$$
\begin{bmatrix}
1 & 0 & 0 & 0 & 0 & 0 & 0 & 0 \\
0 & 1 & x_1^i & y_1^i & 0 & 0 & 0 & 0 \\
. & . & . & . & . & . & . & . \\
1 & 0 & 0 & 0 & 0 & 0 & 0 & 0 \\
0 & 1 & x_n^i & y_n^i & 0 & 0 & 0 & 0 \\
\frac{\lambda\Delta a_{n+1}^i}{4\pi\Delta r_{n+1}^i} & -1 & -x_{n+1}^i & y_{n+1}^i & 0 & 0 & 0 & 0 \\
. & . & . & . & . & . & . & . \\
\frac{\lambda\Delta a_{n+m}^i}{4\pi\Delta r_{n+m}^i} & -1 & -x_{n+m}^i & y_{n+m}^i & 0 & 0 & 0 & 0 \\
0 & 0 & 0 & 0 & 1 & 0 & 0 & 0 \\
0 & 0 & 0 & 0 & 0 & 1 & x_{n+m+1}^{i+1} & y_{n+m+1}^{i+1} \\
. & . & . & . & . & . & . & . \\
0 & 0 & 0 & 0 & 1 & 0 & 0 & 0 \\
0 & 0 & 0 & 0 & 0 & 1 & x_{n+m+p}^{i+1} & y_{n+m+p}^{i+1} \\
1 & 0 & 0 & 0 & -1 & 0 & 0 & 0 \\
0 & 1 & x_{n+m+p+1}^i & y_{n+m+p+1}^i & 0 & -1 & -x_{n+m+p+1}^{i+1} & -y_{n+m+p+1}^{i+1} \\
. & . & . & . & . & . & . & . \\
1 & 0 & 0 & 0 & -1 & 0 & 0 & 0 \\
0 & 1 & x_{n+m+p+q}^i & y_{n+m+p+q}^i & 0 & -1 & -x_{n+m+p+q}^{i+1} & -y_{n+m+p+q}^{i+1}
\end{bmatrix}
\bullet
\begin{bmatrix}
\Phi_0^i \\ b_0^i \\ b_1^i \\ b_2^i \\ \Phi_0^{i+1} \\ b_0^{i+1} \\ b_1^{i+1} \\ b_2^{i+1}
\end{bmatrix}
=
\begin{bmatrix}
\Phi_1^i - \frac{4\pi D_{r_1}^i}{\lambda} \\
\delta_{a_1}^i - D_{a_1}^i \\
\cdots \\
\Phi_1^i - \frac{4\pi D_{r_n}^i}{\lambda} \\
\delta_{a_n}^i - D_{a_n}^i \\
\frac{\lambda\Delta a_{n+1}^i}{4\pi\Delta r_{n+1}^i}\Phi_{n+1}^i - \delta_{a_{n+1}}^i \\
\cdots \\
\frac{\lambda\Delta a_{n+m}^i}{4\pi\Delta r_{n+m}^i}\Phi_{n+m}^i - \delta_{a_{n+m}}^i \\
\Phi_{n+m+1}^{i+1} - \frac{4\pi D_{r_{n+m+1}}^{i+1}}{\lambda} \\
\delta_{a_{n+m+1}}^{i+1} - D_{a_{n+m+1}}^{i+1} \\
\cdots \\
\Phi_{n+m+p}^{i+1} - \frac{4\pi D_{r_{n+m+p}}^{i+1}}{\lambda} \\
\delta_{a_{n+m+p}}^{i+1} - D_{a_{n+m+p}}^{i+1} \\
\Phi_{n+m+p+1}^i - \Phi_{n+m+p+1}^{i+1} \\
\delta_{a_{n+m+p+1}}^i - \delta_{a_{n+m+p+1}}^{i+1} \\
\cdots \\
\Phi_{n+m+p+q}^i - \Phi_{n+m+p+q}^{i+1} \\
\delta_{a_{n+m+p+q}}^i - \delta_{a_{n+m+p+q}}^{i+1}
\end{bmatrix}
\qquad (29)
$$

In the matrix, the upper index of each variable refers to the frame number, while the lower index refers to the sequential identification number of control points and tie points. Totally, there are *2(n+k+p)+m* observation equations. We denote the design matrix on the left side of the equation (28) or (29) by ***A***, the observation vector on the right side by ***b***, and the vector of unknown parameters by ***X***. Then, we have the generic form of the observation equations:

$$\mathbf{AX} = \mathbf{b} \qquad (30)$$

The least-squares solution for the unknown parameters can be obtained by solving normal equations as follows (Mikhail and Ackermann 1976, Press *et al.* 1992, Mikhail *et al.* 2001):

$$\hat{\mathbf{X}} = (\mathbf{A}^{\mathbf{T}}\mathbf{A})^{-1}\mathbf{A}^{\mathbf{T}}\mathbf{b} \qquad (31)$$

where $\boldsymbol{A^T}$ is the transpose of the design matrix and $\boldsymbol{(A^TA)^{-1}}$ is the inverse of the matrix of the normal equations. If the normal equations are close to singular or large round-off errors are involved, the singular value decomposition (SVD) method gives a more reliable solution to the least-squares problem (Press *et al.* 1992). The simultaneous least-squares adjustment is made so that the velocities of tie points fit together as well as possible, and the residual discrepancies at the velocity control points are as small as possible.

For a strip or a block with k image frames, there are $6k$ unknown parameters in case 1 and $4k$ unknown parameters in case 2 to be solved in the adjustment. Therefore, the required minimum number of linearly independent observation equations is $6k+1$ for the case 1 and $4k+1$ for case 2. The observation equations contributed by tie points free us from the stringent need of velocity control points (stationary or non-stationary) and/or flow direction control points for each frame. The simultaneous strip or block adjustment solves one difficult practical problem: for some image frames we are unable to identify a sufficient number of velocity control points. By exploiting tie points in the strip or block adjustment, unknown parameters for those frames without velocity control points can be calibrated based on distant velocity control points in other image frames. In other words, velocity control points in one frame can contribute to the calibration of unknown parameters of other frames through tie points. The incorporation of constraints imposed by tie points also minimizes the discrepancies of velocity measurements derived from adjacent image frames for overlapping areas. The improved consistency makes it possible to create a seamless velocity mosaic. In addition, the integration of all velocity control points within a strip or a block will increase the redundancy of observation equations and constrain the propagation of errors in individual velocity control points.

4. Application Results

The simultaneous least-squares adjustment method proposed above has been successfully applied to the processing of Radarsat-1 interferometric SAR data acquired during the first Antarctic Mapping Mission (AMM-1) in September and October of 1997. Since Radarsat-1 has a 24-day repeat orbit cycle and the AMM-1 lasted for 30 days, the final 6 days of repeat-pass acquisitions provide a large volume of interferometric SAR data for Antarctica (Jezek 1999, 2002). The long

24-day repeat cycle makes the Radarsat InSAR data sensitive to surface motion and is nearly ideal for measuring slow ice motion with the conventional phase unwrapping method. But, the phase unwrapping for Radarsat interferometric data is difficult in fast-moving areas, where the speckle tracking method becomes an effective alternative approach. In the following sections, we report the application results for two study sites in Antarctica. One site is the lower reach of the Lambert Glacier and the Amery Ice Shelf, which represents a fast-moving area. The other site is located in the upper reach of the Recovery Glacier, which represents a relatively slow moving area. These application examples demonstrate the usefulness of ice flow stripes as control points and the benefits of the simultaneous least-squares adjustment with tie points.

4.1. Strip adjustment of velocity measurements from the speckle tracking method

The Lambert Glacier basin and the Amery Ice Shelf were imaged by the Radarsat-1 C-band sensor on September 24, 1997 with a nominal look angle of 27°. The same area was imaged again on October 18, 1997 during a repeat orbit. Figure 4 shows the location of the study area and the coverage of the interferometric SAR data. The image strip consists of 8 consecutive frames of interferometric SAR data pairs. Each frame covers a ground area of 100 km by 100 km, with about 10 km wide overlap between neighboring frames. Due to fast ice motion and relatively high relief, the conventional phase unwrapping method does not work well, and no reliable phase measurements can be made for this site. Therefore, the speckle tracking method is used to derive both the range and azimuth displacements. The cross-correlation is performed using the single look slant range amplitude images. We experimented with different sizes for the match window. Larger window sizes generally produce more and stronger matches, but require greater spacing between adjacent velocity nodes to minimize the correlation of those surface

displacement estimates. An amplitude match was accepted as a successful match based on an experimentally determined correlation threshold of 0.05. We chose an optimal window size of 96 by 96 pixels, which produced a dense coverage of observations. The match only failed in the margins of the ice streams with high shear strain rate, in the central part of the confluence of the Lambert Glacier, the Mellor Glacier, and the Fisher Glacier, and in a small patch toward the front of the Amery Ice Shelf.

The correlation peak was determined by oversampling the correlation surface by a factor 10. The matched points were checked for outliers using a median operator. A match whose estimated range or azimuth offset differs from the median of its surrounding match points by a specified threshold value was flagged as an outlier and discarded. We interpolated good match points into a range offset grid and an azimuth offset grid with a spacing of 200 m. The topography induced component is removed from the range offset grid by using the OSU Digital Elevation Model (DEM) (Liu *et al*. 1999).

(Insert figure 4 near here)

First, we use frame 5095 and frame 5082 to demonstrate the advantages of simultaneous least-squares adjustment over independent frame-by-frame adjustment. Since no *in-situ* velocity measurements are available for this region, we identify rock outcrops and use them as stationary velocity control points. We identify 17 stationary velocity control points for frame 5082 and 16 stationary velocity control points for frame 5095, which are well distributed in both the range and azimuth directions. Following Equation (10) and Equation (11), we wrote 34 observation equations for frame 5082, and 32 observation equations for frame 5095 based on the control points. With overabundant observation equations, we calibrated the unknown parameters a_0, a_1, a_2. b_0, b_1, and b_2 respectively for frame 5082 and frame 5095 as shown in table 1. Using the

calibrated parameters, the motion induced surface displacements in the range and azimuth directions were computed for each grid cell, and the surface velocity for each grid cell was then calculated by using Equations (5) and (6). In the calculation, the surface slopes along the range and azimuth directions were estimated by using the OSU Digital Elevation Model (DEM) (Liu *et al.* 1999).

(Insert table 1 near here)

As shown in figure 5, the spatial pattern of the derived speed appears consistent with glacial features and the flow directions agree well with ice flow stripes in the scene. However, the merged velocity field has an obvious seam line (figure 6a), which indicates a sudden change in velocity between frame 5082 and frame 5095. In fact, the average speed discrepancy between frames is about 6 m/year for the overlapping area.

(Insert figure 5 about here)

With 30 tie points in the overlapping area between two frames, we performed a simultaneous least-squares adjustment. The tie points were initially determined by using ancillary information in the header files and then refined using the cross-correlation matching with sub-pixel level accuracy. Following Equations (23) and (24), we obtained 60 observation equations for the tie points. By combining 17 stationary velocity control points from frame 5082, 16 stationary velocity control points frame 5095, and 30 tie points, we obtained 126 observation equations in a matrix format similar to Equation (28). The unknown parameters a_0, a_1, a_2. b_0, b_1, and b_2 for frame 5082 and frame 5095 were simultaneously computed based on the 126 observation equations, as shown in table 1. The parameters calibrated by the simultaneous least-squares adjustment were used to re-compute the velocity fields for the two frames. The consistency of the estimated velocity between two frames was greatly improved. We calculated

the velocity difference for each pixel in the 10 km wide overlapping area. The average velocity difference has been reduced from 6 m/year to 1.33 m/year, and the standard deviation of the velocity difference has also been reduced from 9.5 m/year to 4.6 m/year. Note that the standard deviation value mainly represents the effect of random noise, and the effect of the simultaneous least-squares adjustment on the reduction of the systematic bias is obviously greater than that of the random error. The simultaneous adjustment achieved a continuous transition of the velocity field between the two frames as evidenced by the seamless velocity mosaic in figure 6b.

(Insert figure 6 about here)

The simultaneous least-squares adjustment method also eliminates the stringent requirement regarding velocity control points for each frame. To demonstrate this desirable property, we dropped the 17 stationary velocity control points for frame 5082, and only employed 16 stationary velocity control points for frame 5095 and 30 tie points. In the course of the simultaneous strip adjustment, the parameters a_0, a_1, a_2. b_0, b_1, and b_2 for frame 5082 were calculated based on the tie points and stationary velocity control points in the adjacent frame 5095. As shown in table 2, the parameters estimated for frame 5082 without using the velocity control points in this frame are very similar to those calculated by using the velocity control points in this frame. The average velocity difference for the entire frame is only 3.2 m/year, compared with the velocity estimates using velocity control points in frame 5082. This demonstrates that the simultaneous least-squares adjustment method is able to derive the velocity measurements for those frames without velocity control points. This is of particular importance for flat featureless snow surfaces such as portions of the Amery Ice Shelf covered by frames 4998 and 4981, where no rock exposures can be found and used as stationary velocity controls.

(Insert table 2 and figure 7 about hear)

Flow direction control points can be used alone or in conjunction with stationary velocity control points in the least-squares adjustment for solving the unknown parameters for a frame. To demonstrate this, we identified 24 flow direction control points for frame 5095 by drawing a line segment along the visible flow stripes on the slant range SAR image. The flow direction control points are shown in figure 7 as line segments, and their positions are marked as circles in the middle of the line segments. Following Equation (16), we established 24 observation equations for the flow direction control points. As shown in figure 7, the flow stripes used for flow direction control have different orientations, which ensure linear independence between the observation equations. By using 24 observation equations derived only from the flow direction control points, we calibrated the parameters for frame 5095. As shown in table 2, the parameter values of a_0, a_1, a_2. b_0, b_1, and b_2 calibrated from the flow direction control points are similar to those calibrated from the stationary velocity control points. The corresponding velocity difference is 8.1 m/year on average for the entire frame, compared with the results from the stationary velocity control points. It should be pointed out that the parameters calibrated by the stationary velocity control points have higher accuracy and should be used whenever they are available. Nevertheless, if stationary velocity control points cannot be identified, flow direction control points can be used instead to derive velocity estimates at a slightly lower but acceptable level of accuracy.

(Insert table 3 and figure 8 about hear)

To derive a seamless velocity mosaic for the entire strip, we performed a unified simultaneous least-squares adjustment of the eight consecutive interferometric frames by integrating stationary velocity control points, flow direction control points and tie points. As shown in table 3, we identified plenty of stationary velocity control points for the five frames on

the left side of the strip, a few stationary velocity control points for frame 5015, and no stationary velocity control points for frame 4998 and frame 4981. Nevertheless, we were able to extract 9 flow direction control points for frame 4998 and 6 flow direction control points for frame 4981. We identified 30 tie points for adjacent frames, resulting in 210 tie points for the entire strip in total. The combination of stationary velocity control points, flow direction control points and tie points from all frames creates observation equations in a similar matrix format as Equation (28). We simultaneously computed the parameters for all eight frames and hence created a seamless velocity mosaic across the entire strip as shown in figure 8. Ice surface velocity is shown as a color overlay. The lower speeds are represented with blue tones, changing to red for the highest speeds. Velocity varies considerably along the glacial floor and the ice shelf. It increases from the interior up to about 800 m/year at the confluence of the Lambert Glacier, the Mellor Glacier and the Fisher Glacier. Then, the velocity decreases to lower values of 300-350 m/year in the middle section and increases to a maximum of about 1470 m/year near the front of the Amery Ice Shelf.

4.2 Strip adjustment of velocity measurements derived from the phase unwrapping method and the speckle tracking method

The Recovery Glacier in East Antarctica was imaged by the Radarsat-1 sensor during AMM-1 two times respectively on September 23 and October 27 of 1997 during repeat orbits. We use two adjacent frames, 5527 and 5544, from this interferometric strip to demonstrate the simultaneous least-squares adjustment of surface displacement measurements derived by coupling the phase unwrapping method and the speckle tracking method. The two interferometric frames cover the upstream reach of the Recovery Glacier (figure 9), which is a

relatively slow moving area with a low snow accumulation rate. Sufficient coherence of interferometric SAR pairs enables us to employ the conventional phase unwrapping method to derive precise measurements on the range displacements. Along with the azimuth displacements derived from the speckle tracking method, highly accurate two-dimensional surface velocity fields for two frames were derived.

(Insert figure 9 about here)

To derive the range displacements, we conducted a sequence of interferometric processing steps on the Single Look Complex (SLC) images of InSAR pairs. First, sub-pixel level co-registration of the two SLC images was performed using a local co-registration method (Zhao 2001). With co-registered complex images, the interferogram and coherence image were calculated. Phase flattening was performed to remove the baseline and topography effects based on the OSU DEM (Liu *et al.* 1999). Goldstein's branch-cut method (Goldstein *et al.* 1988, 1993) was used to unwrap the differential phase. The baseline geometry was also refined with ground control points. After removing the baseline and topography effects, the unwrapped phase measurements are related only to surface motion in the LOS direction. By using the speckle tracking method as described above, we also derived azimuth offset grids for both frame 5527 and frame 5544.

(Insert table 4 near here)

We first performed an independent single frame least-squares calibration to determine parameters for each frame. For frame 5527, we identified 14 stationary velocity control points. Following Equation (11) and Equation (12), we obtained 28 observation equations. The parameter values of Φ_0, b_0, b_1, and b_2 calibrated for frame 5527 by the single frame least-squares adjustment are shown in table 4. Similarly, we calibrated the unknown parameters Φ_0, b_0, b_1, and

b_2 for frame 5544 using 26 stationary velocity control points (table 4). We computed the velocity field for each frame by using Equation (2) and Equation (6). For the 10 km wide overlap area, the velocity differences between the two frames have a mean value of 4.39 m/year and a standard deviation of 6.74 m/year. Again, the velocity difference is caused by the fact that velocity control points for each frame have a different quality and spatial configuration and the imaging geometry for the two frames was also slightly different.

(Insert figure 10a and 10b near here)

To perform a simultaneous strip adjustment, 22 tie points were identified in the overlap area. Observation equations for each tie point were created following Equation (24) and Equation (27). By integrating tie points and stationary velocity control points for both frames, we obtained observation equations in a matrix format similar to Equation (29). The unknown parameters Φ_0, b_0, b_1, and b_2 for frame 5527 and frame 5544 were simultaneously determined in the course of the simultaneous least-squares adjustment. Table 4 lists the calibration results for these parameters. After strip calibration, the mean of the velocity difference for the overlap area has been reduced to 0.55 m/year from 4.39 m/year, and the standard deviation of velocity difference has been also reduced to 4.96 m/year from 6.74. The seamless velocity mosaic in figure 10 suggests that the simultaneous strip adjustment with tie points minimizes the discrepancy of velocity measurements between adjacent frames and enhances the consistency of velocity measurements within the strip.

5. Conclusions

Repeat-pass interferometry has been well established as a precise technique to measure surface motion. Previously, multiple interferometric SAR image frames were commonly processed on a

frame by frame basis to obtain velocity estimates over a large area. This paper presents a simultaneous least-squares adjustment method for calibrating and merging surface displacement measurements derived from individual interferometric SAR pairs within a strip or a block. Observation equations for velocity control points, flow direction control points, and tie points have been mathematically derived in two cases. In the first case, both range and azimuth surface displacements are derived by the speckle tracking method. In the second case, range displacements are derived by the phase unwrapping method and azimuth displacements are derived by the speckle tracking method. Although the simultaneous block adjustment method has long been employed in photogrammetry to process a series of aerial photographs or satellite images into an orthorectified image mosaic (Kraus 1993, Mikhail *et al.* 2001), this paper represents the first detailed treatment of the simultaneous least-squares adjustment method for processing multiple frames of interferometric velocity data.

Mathematical derivation and application examples clearly show that the simultaneous least-squares adjustment method has several advantages over the frame-by-frame processing method. First, it enhances the velocity consistency across the entire strip or block and avoids possible artificial spatial discontinuities of the velocity between frames. Second, it relaxes the requirement for a certain minimum number of velocity control points in each frame. The use of tie points makes it possible to bridge frames that do not have velocity control points. In addition, we demonstrate that ice flow stripes can be utilized as flow direction constraints in the least-squares adjustment. The introduction of this new type of control points further reduces the difficulty and cost associated with the acquisition of stationary and non-stationary velocity control points in practice. Third, the simultaneous least-squares adjustment by integrating all velocity control points and tie points can limit the propagation of errors in the input control

points and hence improve the overall accuracy of velocity measurements across the entire strip or block.

Usually, interferometric SAR data are processed by data suppliers into individual square frames with overlapping areas, although the raw radar data were acquired in a continuous strip. This is because the storage and memory requirements are extremely high for processing interferometric SAR data and most InSAR software packages can only handle individual InSAR frames. However, it should be noted that it is possible to process a long interferometric SAR strip at one time, if one has a SAR processor and software tools to handle an interferometric SAR strip. With strip mode processing, we can avoid strip adjustment for stitching individual frames into a continuous strip. But, the simultaneous least-squares adjustment method would be still useful for calibrating and merging adjacent strips into a block.

Our method has been successfully applied to the processing of multiple frames of interferometric data in Antarctica collected by the Radarsat-1 C-band SAR sensor. It should be emphasized that the observation equations that we derived for the velocity control points, flow direction control points, and tie points are generic and equally applicable to interferometric data collected by other SAR sensors. With the increasing availability of interferometric SAR data, we believe that our simultaneous least-squares adjustment method will find wide practical applications in the future.

Acknowledgment

This work was supported by the National Science Foundation (NSF) grant No. 0126149.

References

BINDSCHADLER, R., and SCAMBOS, T., 1991, Satellite image derived velocity field of an Antarctic ice stream. *Science*, **252**, 242-246.

CASASSA, G., BRECHER, H.H., 1993, Relief and decay of flow stripes on Byrd Glacier, Antarctica. *Annals of Glaciology*, **17**, 255-261.

FAHNESSTOCK, M., BINDSCHADLER, R., KWOK, R., and JEZEK, K., 1993, Greeenland Ice Sheet surface properties and ice dynamics from ERS-1 SAR imagery. *Science*, **262**, 1530-1534.

FATLAND, D.R., and LINGLE, C. S., 1998, Analysis of the 1993-95 Bering Glacier Surge using Differential SAR Interferometry. *Journal of Glaciology*, **44** (148), 532-546.

FROLICH, R.M., AND DOAKE, C.S.M., 1998, Synthetic Aterture Radar Interferometry ove Rutford Ice Stream and Carlson Inlet, Antarctica. *Journal of Glaciology*, **44**(146), 77-92

GOLDSTEIN, R.M., ENGELHARDT, H., KAMB, B., and FROLICH, R., 1993, Satellite radar interferometry for monitoring ice sheet motion: application to an Antarctic ice stream. *Science*, **262**, 1525-1530.

GOLDSTEIN, R.M., ZEBKER, H.A., and WERNER, C.L., 1988, Satellite radar interferometry: two-dimensional phase unwrapping. *Radio Science*, **23**(4), 713-720.

GRAY, A.L., JOUGHIN, I., TULACZYK, S., SPIKES, V. B., BINDSCHADLER, R., and JEZEK, K.C., 2005, Evidence for subglacial water transport in the West Antarctic Ice Sheet through three-dimensional satellite radar interferometry. *Geophysical Research Letter*, **32**, L03501, dio:10.1029/2004GL021387.

GRAY, A.L., MATTER, K.E., VACHON, P.W., BINDSCHADLER, R., JEZEK, K.C., FORSTER, R., and CRAWFORD, J.P., 1998, InSAR results from the RAMP data:

estimation of Glacier motion using a simple registration procedure. *IGARSS'98*, Vol. 3, 1638-1640, Seattle, WA, July 1998.

GRAY, A.L., SHORT, N., MATTER, K.E., and JEZEK, K.C., 2001, Velocities and Ice Flux of the Filchner Ice Shelf and its Tributaries determined from Speckle Tracking Interferometry. *Canadian Journal of Remote Sensing*, **27**(3), 193-206.

HAMILTON, G.S. AND WHILLANS, I.M., 2000, Point measurements of mass balance of the Greenland ice sheet using precision vertical global positioning system (GPS) surveys. *Journal of Geophysical Research*, **105**, 16,295-16,301.

JEZEK, K.C., 1999, Glaciologic properties of the Antarctic Ice Sheet from spaceborne Synthetic Aperture Radar observations. *Annals of Glaciology*, **29**, 286-290.

JEZEK, K.C., 2002, RADARSAT-1 Antarctic Mapping Project: change detection and surface velocity campaign. *Annals of Glaciology*, **42**(142), 564-575.

JOUGHIN, I., 2002, Ice-sheet velocity mapping: a combined interferometric and speckle-tracking approach. *Annals of Glaciology*, **34**, 195-201.

JOUGHIN, I., FAHNESTOCK, M., KWOK, R., GOGINENI, P., and ALLEN, C., 1999a, Ice flow of Humboldt, Petermann and Ryder Gletscher, Greenland. *Journal of Glaciology*, **45**(150), 231-241.

JOUGHIN, I., GRAY, L., BINDSCHADLER, R., PRICE, S., MORSE, D., HULBE, C., MATTAR, K., and WERNER, C., 1999b, Tributaries of West Antarctic Ice Streams revealed by Radardsat interferometry. *Science*, **286**, 283-286.

JOUGHIN, I., KWOK, R. and FAHNESTOCK, M., 1996, Estimation of ice-sheet motion using satellite radar interferometry: method and error analysis with application to Humboldt Glacier, Greenland. *Journal of Glaciology*, **42** (142), 564-575.

JOUGHIN, I., KWOK, R. and FAHNESTOCK, M., 1998, Interferometric estimation of three dimensional ice-flow using ascending and descending passes. *IEEE Trans. Geoscience and Remote Sensing*, 36(1), 25-37.

JOUGHIN, I., WINEBRENNER, D., FAHNESTOCK, M., KWOK, R. and FRABILL, W., 1996, Measurement of ice-sheet topography using satellite-radar interferometry. *Journal Glaciology*, **42** (140), 10-22.

KIERNAN, R., 1998, Ice sheet surface velocities along the Lambert Glacier Basin Traverse Route. *Antarctic CRC Research Report No.10*, Australian Antarctic Division.

KING, M., NGUYEN, L., COLEMAN, R., AND MORGAN, P.J., 2000, Strategies for high precision processing of GPS measurements with application to the Amery Ice Shelf, East Antarctica. *GPS Solutions*, **4**(1), 2-12.

KRAUS, K., 1993, *Photogrametry: Fundamentals and Standard Processes*, Volume 1, Fourth Revised and Enlarged Edition, 397p (Bonn: Seiten-Dummlers).

KWOK, R. and FAHNESTOCK, M., 1996, Ice sheet motion and topography from radar interferometry. *IEEE Transactions on Geoscience and Remote Sensing*, **34** (1), 189-199.

LIU, H., JEZEK, K., LI, B., 1999, Development of Antarctic Digital Elevation Model by Integrating Cartographic and Remotely Sensed Data: A GIS-based Approach. *Journal of Geophysical Research*, **104**(B10):23,199-23,213.

LUCCHITTA, B.K., AND FERGUSON, H.M., 1986, Antarctica: measuring glacier velocity from satellite images, *Science*, **234**, 1105-1108.

MICHEL, R and RIGNOT, E., 1999, Flow of glaciar Moreno, Argentina, from repeat-pass shuttle imaging radar images: comparison of the phase correlation method with radar interferometry. *Journal of Glaciology*, **45**(149), 93-100.

MIKHAIL, E.D. and ACKERMANN, F.E., 1976, *Observations and Least-squares* (New York: Dun-Donnelley).

MIKHAIL, E.M., Bethel, J.B., MCGLONE, J.C., 2001, *Introduction to Modern Photogrammetry,* 479p (New York: John Wiley & Sons, Inc.).

MOHR, J.J., REEH, N., AND MADSEN, S.N., 1998, Three-dimensional glacial flow and surface elevation measured with radar interferometry, *Nature*, **391**, 273-276.

PRESS, W.H., TEUKOLSKY, S.A., VETTERLING, W. T., and FLANNERY, B.P., 1992, *Numerical Recipes in C: the Art of Scientific Computing*, Second Edition (Cambrige: Cambridge University Press).

RIGNOT, E., 1996, Tidal motion, ice velocity and melt rate of Petermann Gletscher, Greenland, measured by SAR interferometry. *Journal of Glaciology*, **42**(142), 476-485.

RIGNOT, E., 2002, Mass balance of East Antarctic glaciers and ice shelves from satellite data. *Annals of Glaciology*, **34**, 217-227.

SCAMBOS, T.A., AND BINDSCHADLER, R., 1993, Complex ice stream flow revealed by sequential satellite imagery. *Annals of Glaciol.*, **17**, 177-182.

SCAMBOS, T.A., DUTKIEWICZ, M.J., WILSON, J.C., AND BINDSCHADLER, R., 1992, Application of image cross-correlation to the measurement of glacier velocity using satellite image data. *Remote Sensing of Environment,* **42**, 177-186.

STENOIEN, M.D., AND BENTLEY, C.R., 2000, Pine Island Glacier, Antarctica: a study of the catchment using interferometric Synthetic Aperture Radar measurements and radar altimetry. *Journal of Geophysical Research*, **105** (B9), 21761-21779.

YOUNG, N. and HYLAND, G., 2002, Velocity and strain rates derived from InSAR analysis over the Amery Ice Shelf, East Antarctica. *Annals of Glaciology*, **34**, 228-234.

ZHAO, Z., 2001, *Surface Velocities of the East Antarctic Ice Streams from Radarsat-1 Interferometric Synthetic Aperture Radar Data*. Ph.D. Dissertation, The Ohio State University, Columbus, Ohio.

Figure Captions:

Figure 1: Geometry configuration of repeat-pass interferometry and terrain surface.

Figure 2: Acquisition of a flow direction control point based on an ice flow stripe.

Figure 3: Strip adjustment of two consecutive frames with velocity control points and tie points.

Figure 4: Data coverage of Radarsat interferometric data over the Lambert Glacier and the Amery Ice Shelf acquired in 1997.

Figure 5: Two-dimensional velocity fields derived by the speckle tracking method. (a) frame 5082; (b) frame 5095.

Figure 6: Velocity mosaic of frames 5082 and 5095. (a) processed by the frame-by-frame method; (b) processed by the simultaneous adjustment method

Figure 7: Flow direction control points identified for frame 5095 based on visible ice flow stripes

Figure 8: A seamless velocity mosaic over the Lambert Glacier and the Amery Ice Shelf derived by the unified least-squares adjustment

Figure 9: Locations of interferometric SAR frames 5527 and 5544 over the upper stream of the Recovery Glacier, Antarctica.

Figure 10: Velocity mosaic of frames 5527 and 5544 derived by coupling the phase unwrapping method and the speckle tracking method. (a) processed by the frame-by-frame method; (b) processed by the simultaneous least-squares adjustment.

Table captions:

Table 1: Comparison of model parameters of frames 5082 and 5095 calibrated by the frame-by-frame method and the simultaneous adjustment method

Table 2: Model parameters for frame 5095 derived respectively without using its own velocity control points and using flow direction control points

Table 3: The number of velocity control points and flow direction control points used in the unified least-squares adjustment of eight interferometric data frames over the Lambert Glacier and the Amery Ice Shelf.

Table 4: Comparison of model parameters of frames 5527 and 5544 calibrated by the frame-by-frame method and the simultaneous adjustment method.

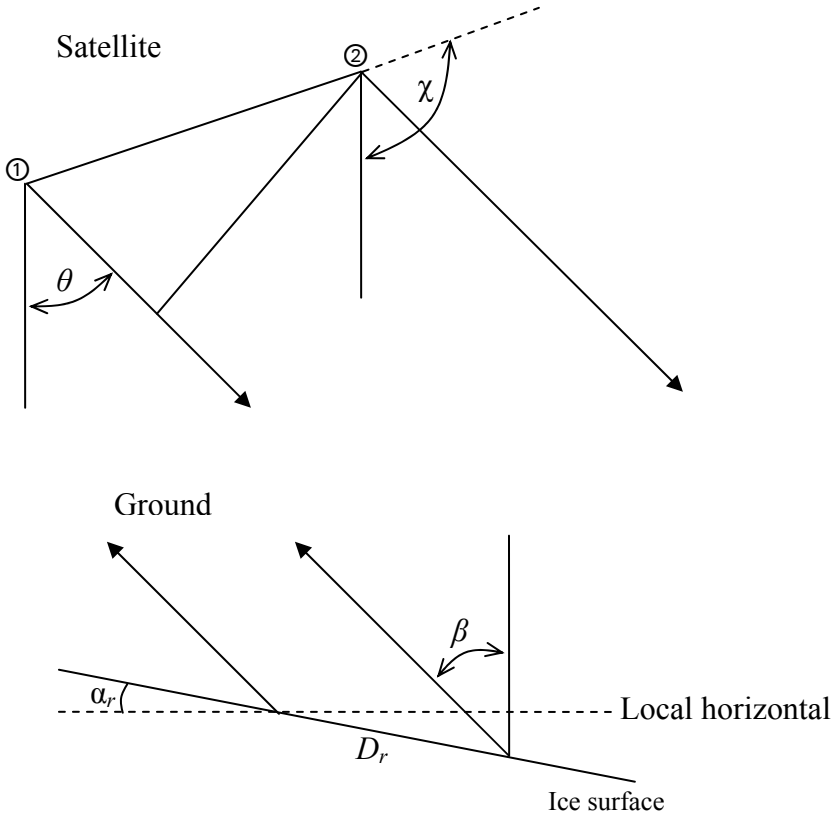

Figure 1: Geometry configuration of repeat-pass interferometry and terrain surface.

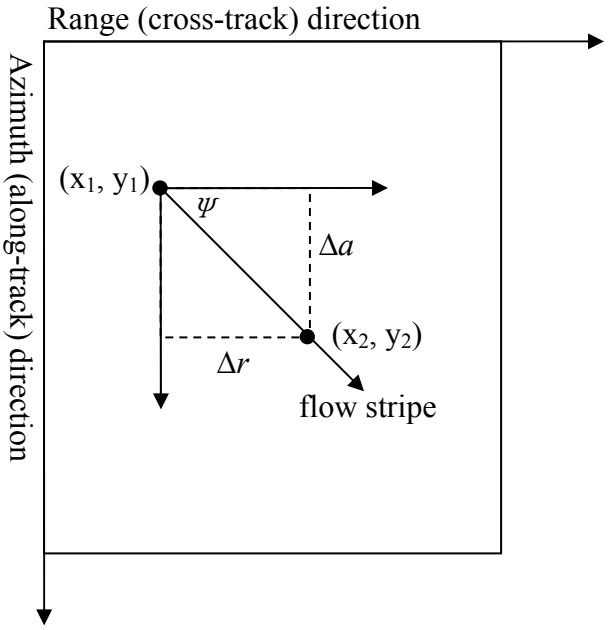

Figure 2: Acquisition of a flow direction control point based on an ice flow stripe.

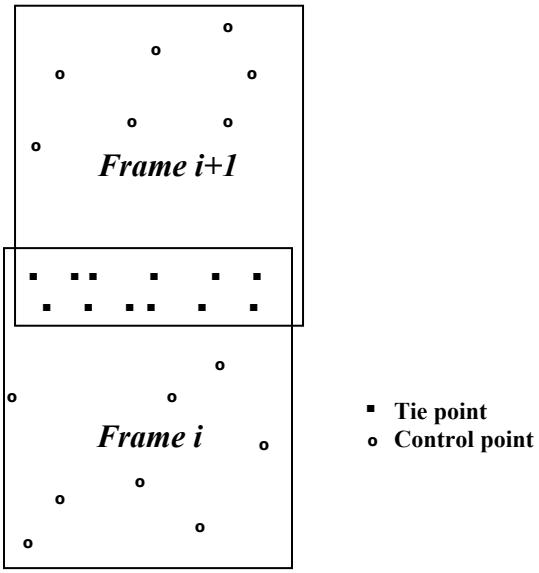

Figure 3: Strip adjustment of two consecutive frames with velocity control points and tie points.

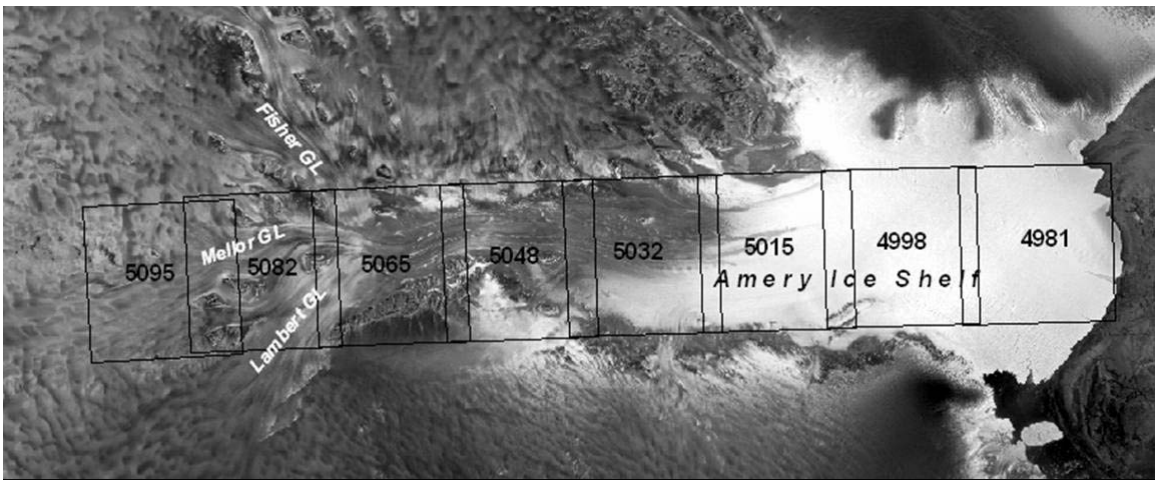

Figure 4: Data coverage of Radarsat interferometric data over the Lambert Glacier and the Amery Ice Shelf acquired in 1997.

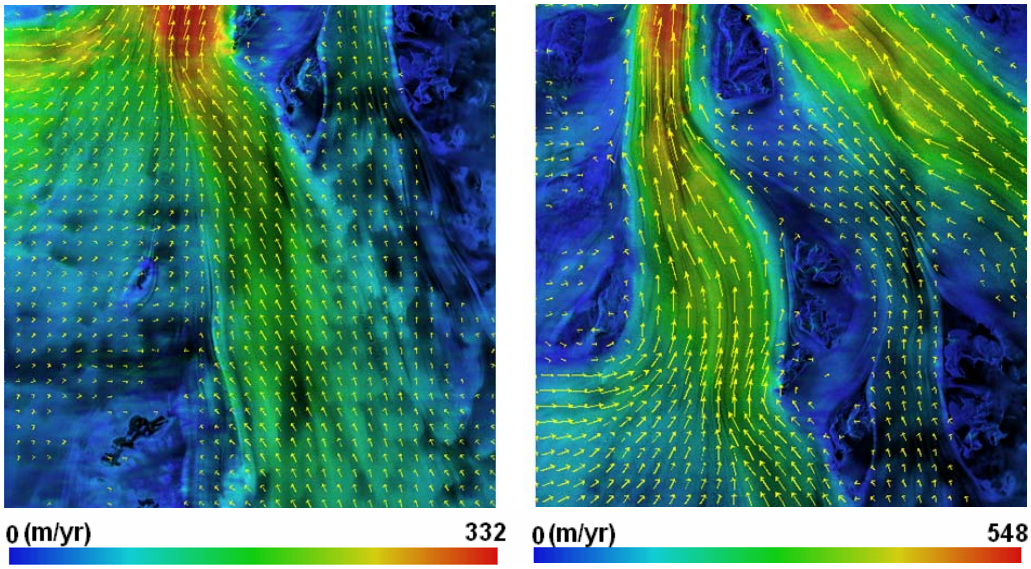

(a) (b)

Figure 5: Two-dimensional velocity fields derived by the speckle tracking method. (a) frame 5082; (b) frame 5095.

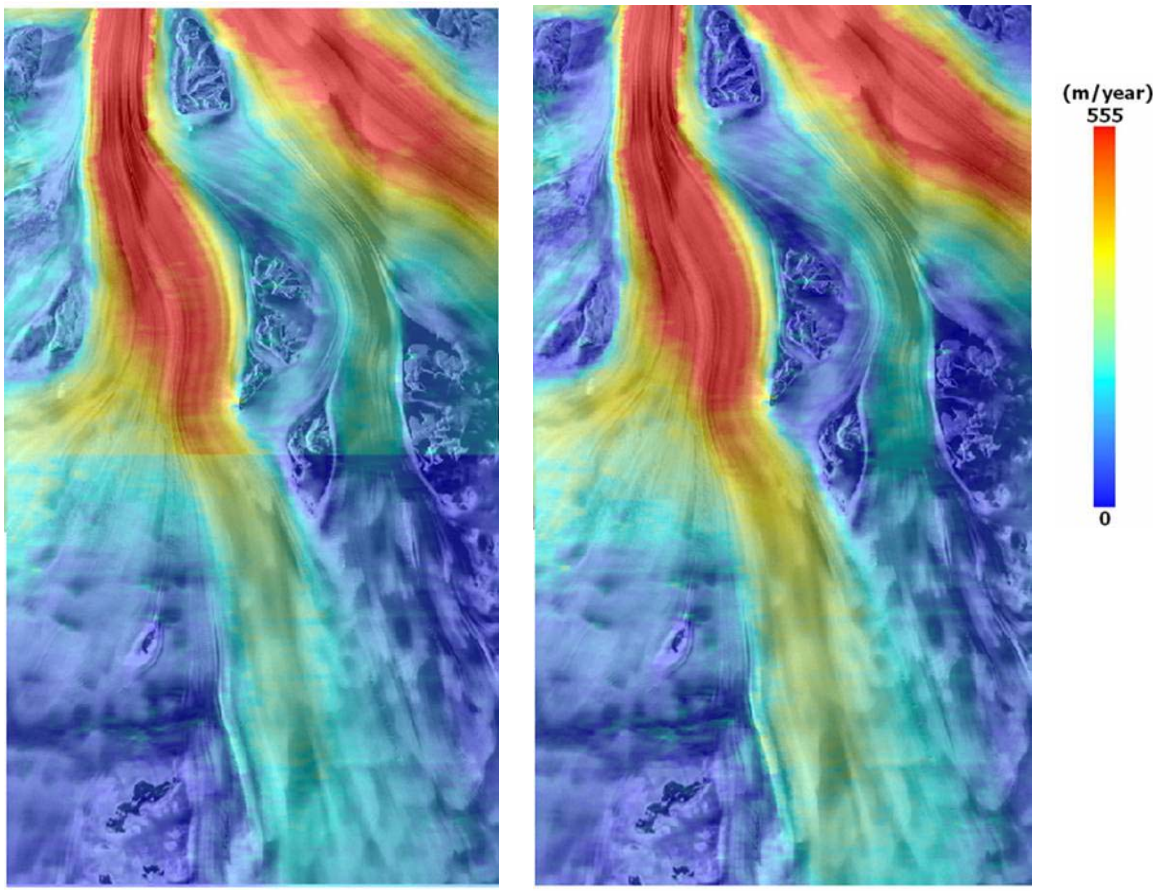

Figure 6: Velocity mosaic of frames 5082 and 5095. (a) processed by the frame-by-frame method; (b) processed by the simultaneous adjustment method

Figure 7: Flow direction control points identified for frame 5095 based on visible ice flow stripes

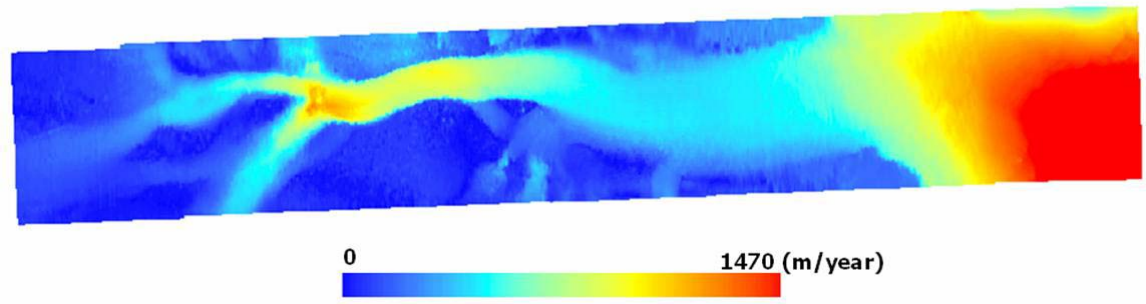

Figure 8: A seamless velocity mosaic over the Lambert Glacier and the Amery Ice Shelf derived by the unified least-squares adjustment

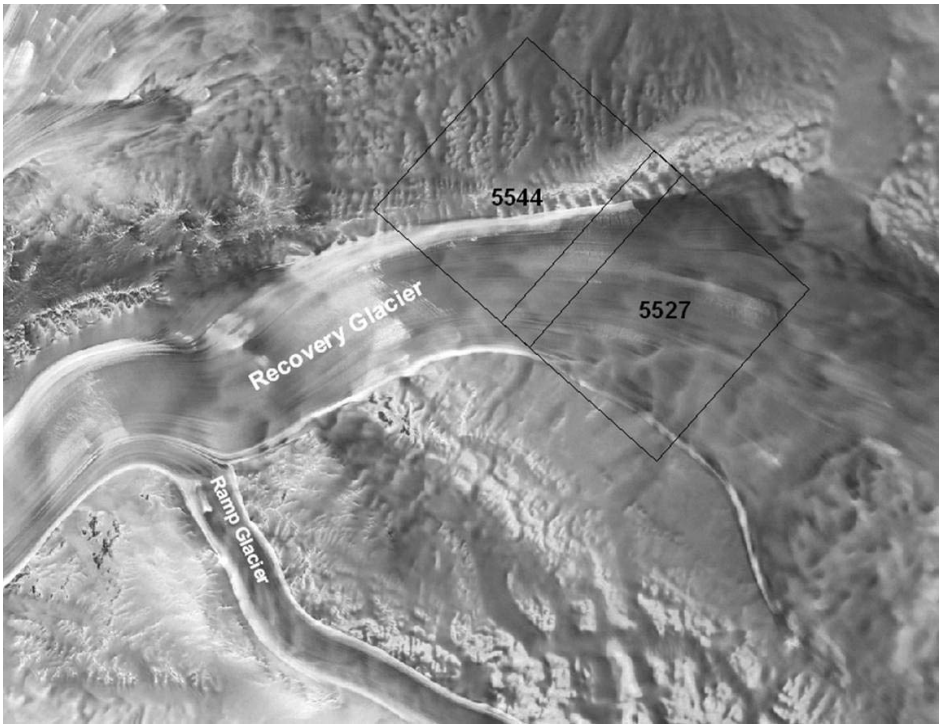

Figure 9: Locations of interferometric SAR frames 5527 and 5544 over the upper stream of the Recovery Glacier, Antarctica.

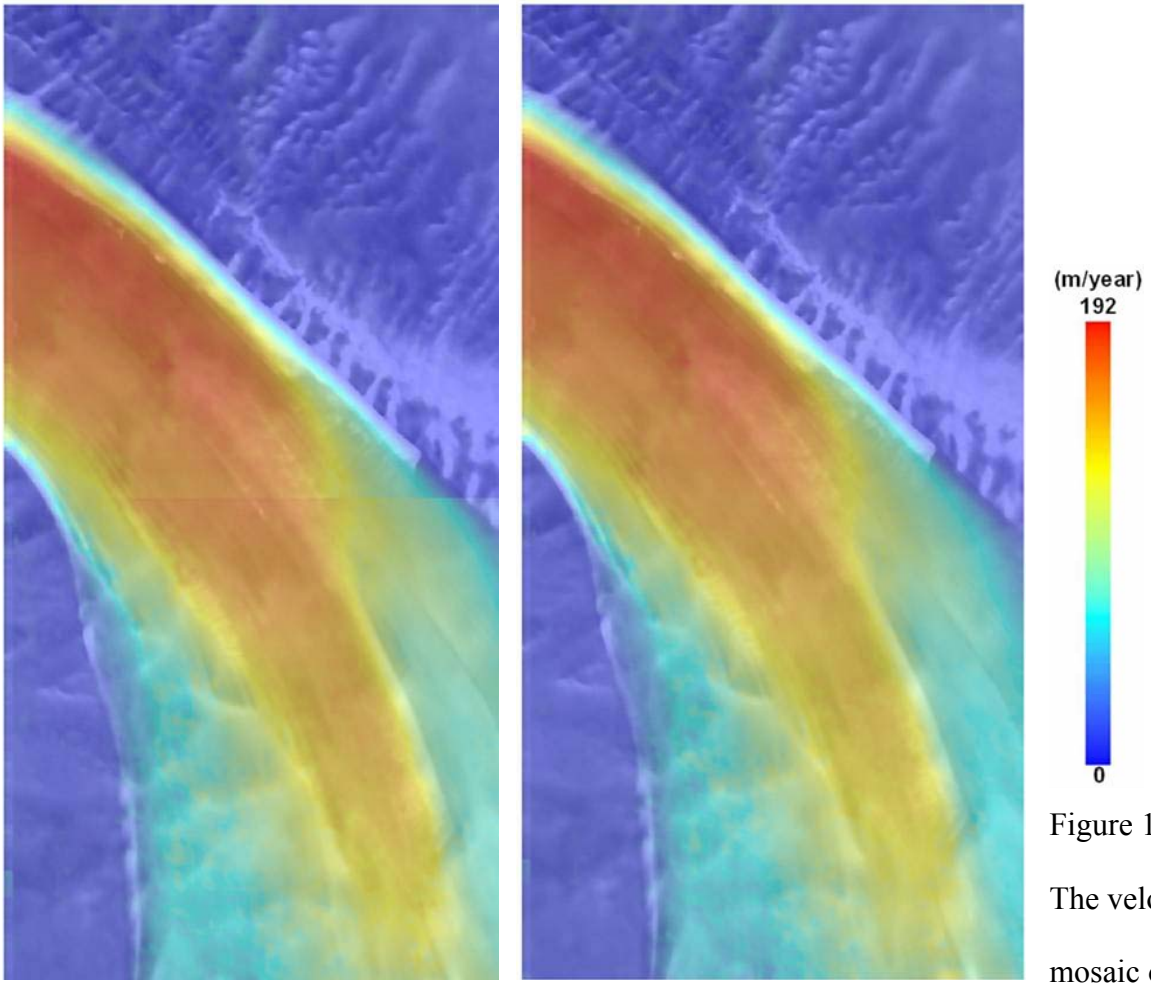

Figure 10: The velocity mosaic of frames 5527 and 5544 derived by coupling the phase unwrapping method and the speckle tracking method. (a) processed by the frame-by-frame method; (b) processed by the simultaneous least-squares adjustment.

Table 1: Comparison of model parameters of frames 5082 and 5095 calibrated by the frame-by-frame method and the simultaneous adjustment method

Model parameters	Frame-by-frame calibration		Simultaneous calibration	
	Frame 5095	Frame 5082	Frame 5095	Frame 5082
a_0	-7.77726	-1.22928	-7.61446	-1.25436
a_1	-0.000225	-0.000278	-0.000257	-0.000267
a_2	-0.0000074901	-0.0000143081	-0.0000127392	-0.0000154897
b_0	-88.9	412.4678	-88.83	412.5
b_1	0.0001488	0.0001197	0.0001361	0.0001225
b_2	0.0000181	0.000001494	0.00001546	0.0000013

Table 2: Model parameters for frame 5095 derived respectively without using its own velocity control points and using flow direction control points

Model parameters	Without velocity control points from frame 5095	Using flow direction control points in frame 5095
a_0	-7.53359	-7.67819
a_1	-0.000278	-0.00024
a_2	-0.0000131975	-0.0000141040
b_0	-88.78	-88.7485
b_1	0.00013	0.0001405
b_2	0.000007757	-0.000005634

Table 3: The number of velocity control points and flow direction control points used in the unified least-squares adjustment of eight interferometric data frames over the Lambert Glacier and the Amery Ice Shelf.

Frame	Stationary velocity control points	Flow direction control points
5095	16	0
5082	17	0
5065	15	0
5048	18	0
5032	14	0
5015	3	14
4998	0	9
4981	0	6

Table 4: Comparison of model parameters of frames 5527 and 5544 calibrated by the frame-by-frame method and the simultaneous adjustment method.

Model parameters	Frame-by-frame calibration		Simultaneous calibration	
	Frame 5527	Frame 5544	Frame 5527	Frame 5544
Φ_0 (radian)	-400.379	-260.424	-358.734	-274.013
b_0 (pixel)	4.2529	-1.99040331	4.28945	-2.001547
b_1 (pixel/pixel)	0.00011947	0.00010841	0.00011416	0.00011021
b_2 (pixel/pixel)	-0.00000379	0.00000114	-0.00000475	0.0000014